Lone pair induced 1D character and weak cation–anion interactions: Two ingredients for low thermal conductivity in mixed-anion metal chalcohalide CuBiSCl_2

Xingchen Shen, Koushik Pal, Paribesh Acharyya, Bernard Raveau, Philippe Boullay, Oleg Lebedev, Carmelo Prestipino, Susumu Fujii, Chun-Chuen Yang, I-Yu Tsao, et al.

Supplemental Information

Lone Pair Induced 1D Character and Weak Cation-anion Interactions: Two Ingredients for Low Thermal Conductivity in Mixed-anion Metal Chalcohalide $CuBiSCl_2$

Xingchen Shen,[1*] Koushik Pal,[2] Paribesh Acharyya,[1,3] Bernard Raveau,[1] Philippe Boullay,[1] Oleg I. Lebedev, [1] Carmelo Prestipino,[1] Susumu Fujii,[4] Chun-Chuen Yang,[5] I-Yu Tsao,[6] Adèle Renaud,[7] Pierric Lemoine,[8] Christophe Candolfi,[8] Emmanuel Guilmeau[1*]

[1]*CRISMAT, CNRS, Normandie Univ, ENSICAEN, UNICAEN, 14000 Caen, France*

[2]*Dept. of Physics, Indian Institute of Technology Kanpur, Kanpur, UP 208016, India*

[3]*Department of Chemistry, Northwestern University, Evanston, IL 60208, United States*

[4]*Department of Materials, Faculty of Engineering, Kyushu University, Fukuoka 819-0395, Japan*

[5]*Department of Physics, National Central University, Chung-Li District, Taoyuan City, 320317, Taiwan*

[6]Institute of Materials Science and Engineering, National Central University, Jhongli City, *Taoyuan County, 32001, Taiwan*

[7]*Univ Rennes, ISCR–UMR 6226, CNRS, F-35000 Rennes, France*

[8]*Institut Jean Lamour, UMR 7198 CNRS – Université de Lorraine, 54011 Nancy, France*

**Corresponding authors:*xingchen.shen@ensicaen.fr

emmanuel.guilmeau@ensicaen.fr

Experimental Section

Synthesis

The stoichiometric amounts of the starting precursors CuCl (powder, 99%), $BiCl_3$ (powder, 99.9%), Bi (powder, 99.5%), with a 10 wt.% excess S (powder, 99.5%) were weighted and grinded into fine powders inside of an Ar-filled glove box. The fine powders were cold-pressed into pellets and loaded into a carbon coated silica tube, which was then evacuated and sealed at a vacuum of ~10^{-3} Pa. The sealed tube was heated to 703 K within 10 hours and held at this temperature for another 24 hours. Subsequently, it was slowly cooled down to 473 K, followed by annealing at this temperature for 48 hours before turning off the furnace. The obtained ingot was grinded into a fine powder and loaded into a 10 mm graphite die, followed by densification using spark plasma sintering (SPS) at 603 K for 5 minutes under a pressure of 100 MPa. The corresponding SPS-ed sample was verified as highly densified pellet with a 97 % of the theoretical value.

X-ray Diffraction and Stability measurement

High-resolution PXRD data of the synthesized SPS-ed powder were collected at 300 K employing a PANalytical XPert2 system with Cu Kα1/ Kα2 radiation (λ1=1.540598 Å, λ2=1.544426 Å). Rietveld refinement was performed using FullProf[1] and WinPlotr[2] software packages starting from the structural model reported by Ruck *et al*.[3] Zero-point shift, unit cell, peak shape, and asymmetry parameters were refined, as well as atomic coordinates and Biso values of each atoms. Finally, a weak Lorentzian component was refined to correct some broadening effect related to anisotropic particle size (i.e. size model 4 implemented in FullProf). The stability of the synthesized SPS-ed powder was assessed by placing it in ambient air and keeping it inside of glove box for several weeks, respectively, while conducting PXRD testing at regular intervals. X-ray diffraction measurement on a selected single crystal (dimensions: 0.070 ×0.058×0.035 mm^3) from 80 to 300 K using a Rigaku Synergy S diffractometer, equipped with a micro-focus sealed X-ray Mo tube and an Eiger 1M Dectris photon counting detector. Data integration for the single crystal was carried out using the CrysAlisPro software suite. A semi-empirical absorption correction and scaling, leveraging symmetry-equivalent and redundant data, were applied using SCALE3 ABSPACK. The structure was determined through charge flipping,[4] followed by least-squares refinement as implemented in JANA2020.[5]

3D Electron Diffraction

Precession-assisted 3D electron diffraction (ED) datasets were acquired utilizing a JEOL F200 transmission electron microscope operating at 200 kV. The microscope was equipped with an ASI Cheetah M3 detector and a Nanomegas Digistar precession unit. A powder sample, obtained from a $CuBiSCl_2$ pellet, underwent further grinding in ethanol using an agate mortar. Subsequently, drops of the resulting solution were deposited onto a holey carbon membrane supported by a Cu meshed grid. Precession-assisted electron diffraction (PED) patterns were captured using the Instamatic program,[6] employing a precession angle of 1.25° and a tilt step of approximately 1° between each PED pattern. To ensure the robustness of the results, a total of six $CuBiSCl_2$ crystals were utilized. Data processing was carried out using PETS 2.0,[7] and structure refinements were conducted in Jana2020,[5] accounting for both dynamical diffraction and precession effects. Details regarding data reduction and the outcomes of dynamical structure refinement are provided for one selected dataset in Tables 1 and 2.

Maximum Entropy Method and Bond Valence Energy Landscape Calculations

Phased intensity coming from Jana2020 refinement has been analyzed using MEM as implemented in Dysnomia code[8] in order to obtain electron-density distributions. Due the dynamic refinement, several reflection were present more than one time the input file for MEM, in such case their values has been averaged and the error was estimated on the base of the standard deviation of the set. Bond Valence energy landscape has been calculated using as input file the structure resulting from dynamic refinement using BondStr code.[9]

Transmission and Scanning Electron Microscopy

Transmission electron microscopy (TEM), ED, high-angle annular dark-field scanning transmission electron microscopy (HAADF-STEM), and energy dispersive x-ray spectroscopy (EDXS) elemental mapping experiments were carried out on double (probe and image) aberration corrected cold FEG JEM ARM200F microscope operated at 200 kV and equipped with a CENTURIO EDX detector, an ORIUS Gatan camera and Quantum GIF. The TEM specimen was prepared by mechanical grinding samples in ethanol and depositing the obtained suspension on Ni carbon holey grid. Scanning electron micrographs and electron energy dispersive spectroscopy (EDS) analyses were obtained using a JEOL JSM 7200F SEM equipped with an EDX X-Flash Bruker detector.

Heat Capacity and Thermal Conductivity Measurements

The high-temperature thermal conductivity (κ) was estimated utilizing the formula $\kappa = \rho C_p d$. The thermal diffusivity (d) was measured employing a Netzsch LFA 457 laser flash system under a nitrogen atmosphere from 300 to 573 K. C_p measurements were conducted in the temperature range of 2 to 40 K using a conventional relaxation method with the dedicated ^{4}He option of the PPMS. The theoretical C_p above RT for $CuBiSCl_2$ is 0.33 J/g/K under Dulong−Petit approximation, and the density (ρ) was determined via the Archimedes method. κ has an estimated measurement uncertainty of 11%.[10]

Sound Velocity Measurements

The longitudinal and transverse sound velocities at 300 K were measured using the pulse-echo method. A small quantity of grease was applied to ensure effective contact between the sample and the piezoelectric transducers.

Optical Measurements

The UV-vis-NIR diffuse reflectance spectra were recorded with a V-770 JASCO spectrophotometer equipped with an integrated reflectance sphere accessory. The reflectance measurements were made in a wavelength range of 200 to 2500 nm with a 1 nm step on. The optical band gaps (E_g) were determined *via* the absorption/back scattering ratio (K/S) calculated from the raw reflectance data using the $F(R) = K/S = (1 - R)^2/(2R)$ Kubelka−Munk transform.

First-principles Calculations

We performed first-principles calculations based on density functional theory (DFT) calculations using the Vienna Ab-initio Simulation Package (VASP)[11-12] and the projector augmented wave (PAW)[13-14] method. We utilized the PBE generalized gradient approximation (GGA)[15] to treat the exchange-correlation energy of the electrons and used a kinetic energy cut-off of 520 eV. Brillouin zone integrations were performed with k-point mesh of 10 × 10 × 8 for the relaxation of the cell parameters as well as for the static calculations. We included the van der Waals interactions in the calculation with Grimme's correction.[16] The optimized lattice parameters (a = 4.055 Å, b = 12.588 Å, c = 8.462 Å) agree well with the corresponding experimental values (a = 3.966 Å, b = 12.811 Å, c = 8.602 Å). We calculated the harmonic phonon dispersion of $CuBiSCl_2$ using the using the finite-displacement method (also known as the frozen phonon method) in Phonopy,[17] where the displaced configurations were generated using 2×2×2

supercell (containing 80 atoms) of the primitive unit cell (with 10 atoms). For phonon calculations, we used 5×5×4 mesh of k-points while calculating the total energy and forces. The calculated phonon dispersion exhibited several unstable phonon modes that span almost the entire Brillouin zone. We examined some of these unstable phonon modes (with frequencies -38 cm^{-1}, -29 cm^{-1}, and -15 cm^{-1}) by visualizing their eigenvectors at Γ point (**Figs. S5a-c** in SI), which reveal that Cu atoms' vibrations dominate them. Next, we took the strongest unstable phonon mode (-38 cm^{-1}) at Γ point and calculated its potential energy surface, which shows a double-well structure (**Fig. S4** in SI). However, the depth of the well is 5 meV/cell, which is small, signifying relatively weak nature of the unstable phonon mode. We then took the structure, which stays at the minimum of the potential energy well, optimized the structure which lowers its symmetry (*Ama2*) from the parent high-symmetry phase (*Cmcm*). We calculated the phonon dispersion of this re-optimized structure following the same procedure before. In this newly calculated phonon dispersion, all unstable phonon modes disappear and become stable which is shown in the manuscript. A tiny segment of the first phonon branch shows negative values close to Γ point along the Γ-X line, which we believe is an artifact of the calculations and may disappear if we consider larger supercell in the calculations. However, large supercell will make the calculations computationally very expensive and hence we have not attempted it. The high-symmetry points in the Brillouin zone are taken from Setyawan's work.[18] Subsequent calculations are performed taking this lower-symmetry (*Ama2*) dynamically stable structure. We determined the mode Grüneisen parameters of $CuBiSCl_2$ using a finite difference method where we have calculated the phonon frequencies of the compound at two different volumes ($1.02\times V_0$ and $0.98\times V_0$, with V_0 being the equilibrium unit cell volume) and utilized the formula $\gamma_{qv} = -\, d\ln(\gamma_{qv})/d\ln(V)$ where γ_{qv} and V denote Grüneisen parameter and unit cell volume, respectively. We calculated the bulk (B) and shear (G) moduli of $CuBiSCl_2$ using the elastic tensor obtain from first-principles calculations and utilizing Voigt's formula[19]. The longitudinal (ν_L) and transverse (ν_T) sound velocities are obtained using $v_L = \sqrt{\frac{G}{\rho}}$ and $v_T = \sqrt{\frac{(B+\frac{4}{3}G)}{\rho}}$, respectively, where ρ is the density of the compound. The ν_a is calculated using the relation: $\frac{3}{v_a^3} = (\frac{1}{v_L^3} + \frac{2}{v_T^3})$. We used the LOBSTER code [20-21] to analyze the bonding, antibonding and nonbonding interactions between the atoms using the crystal orbital Hamilton population (COHP) method.

Lattice thermal conductivity tensor was calculated using phono3py.[22-23] Third-order interatomic force constants were derived by introducing atomic displacements of 0.05 Å into the supercells. 3×1×2

supercells of the conventional unit cell, which have cell lengths larger than 12 Å and contains 120 atoms, were used to avoid the interactions of displaced atoms beyond the periodic boundaries. Total number of displacements needed for thermal conductivity calculations is 11012. To reduce computational costs, we employed a kinetic energy cut-off of 420 eV and a 2×2×2 Monkhorst-Pack mesh of *k*-points[24] in the force calculations. Note that we preliminarily confirmed that these conditions have negligible influence on the accuracy of the calculated forces. The lattice thermal conductivity tensor was calculated using Boltzmann transport equation with the single mode relaxation time approximation, using a fine *q*-point mesh of 21×27×27 for the first Brillouin zone of the primitive cell. The calculated values of κ_L are 0.29-0.15 W/m/K on average from 300 to 573 K (**Fig. S13**), being underestimated compared to the measured values of 0.9-0.6 W/m/K. This underestimation is probably due to the crystal structure of $CuBiSCl_2$ used in the phonon calculations which was less symmetric (space group *Ama2* with displaced Cu^+ ions) than the experimentally observed structure (*Cmcm*). A more symmetric *Cmcm* structure may be stabilized by anharmonic vibrations at finite temperature and increase κ_L in experiments.

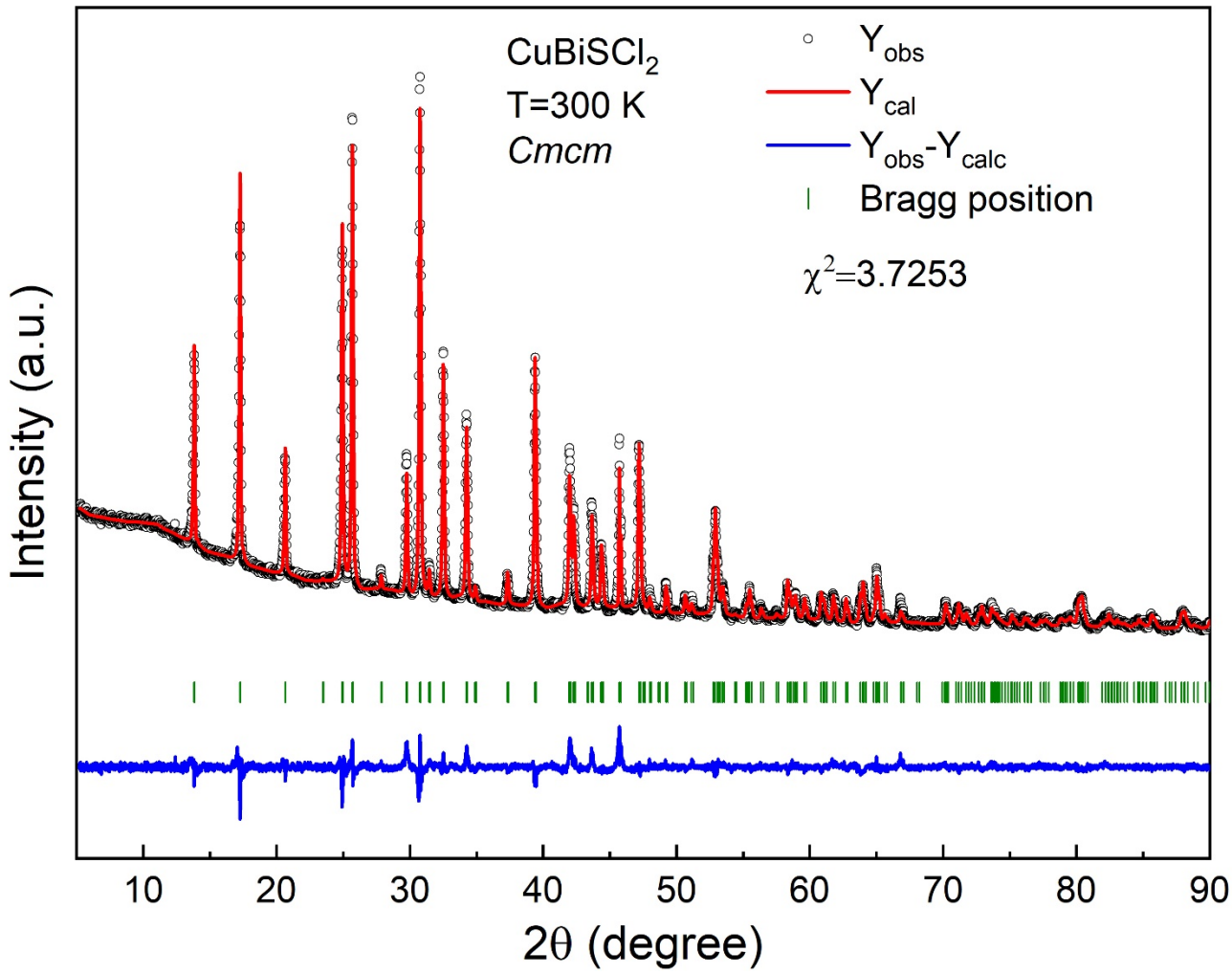

Fig. S1 The refined PXRD of the synthesized $CuBiSCl_2$ powder sample after sintering.

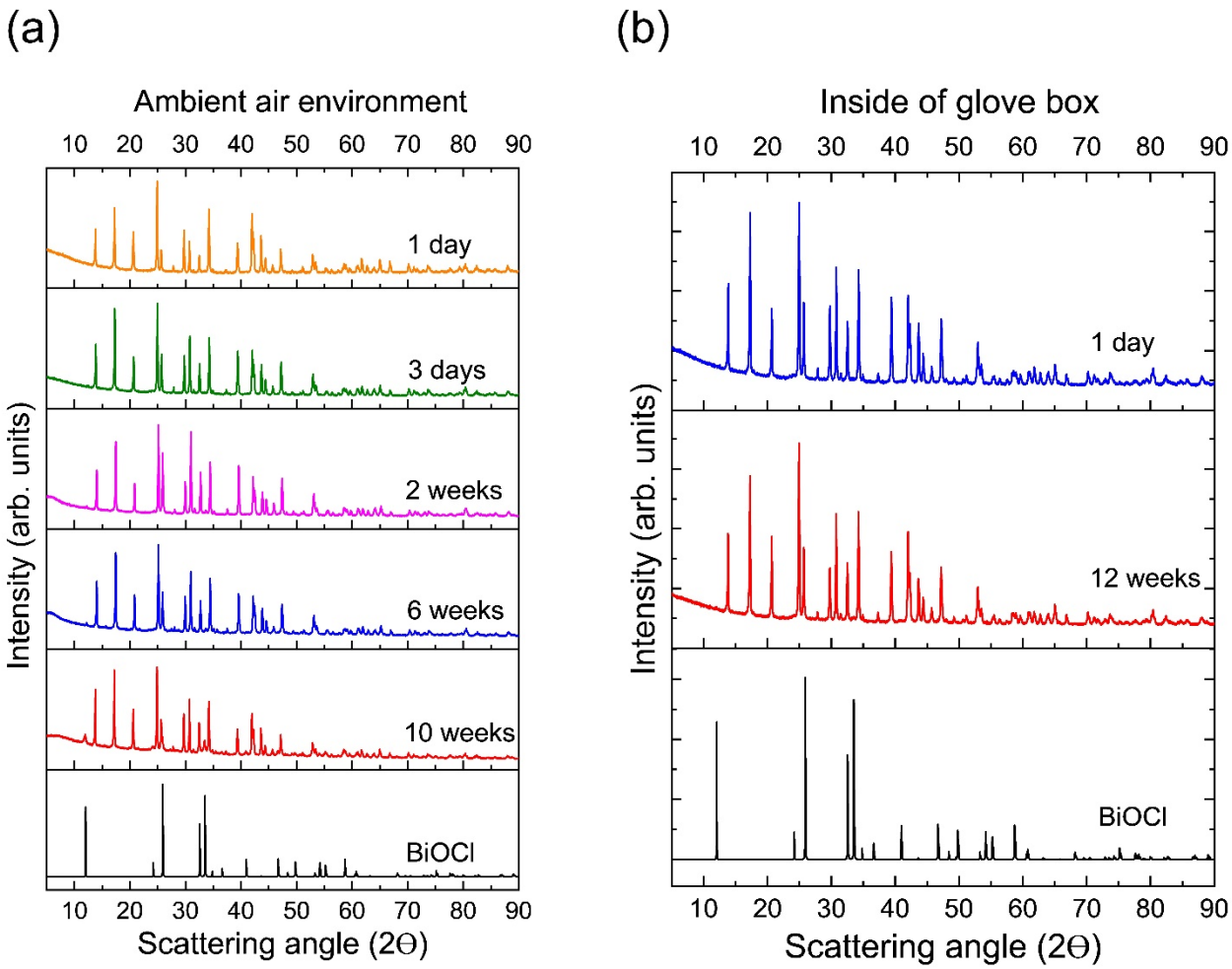

Fig. S2 The PXRD patterns of the $CuBiSCl_2$ powder sample at (a) ambient air environment and (b) inside of glove box at 300 K.

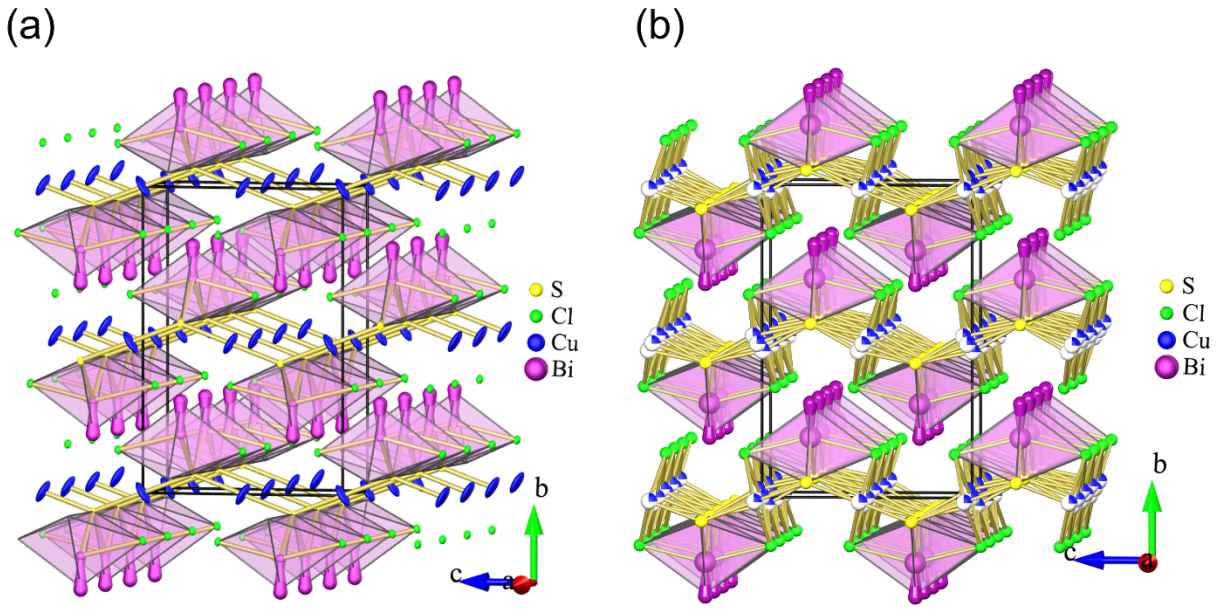

Fig. S3 The structure of $CuBiSCl_2$ with (a) large anisotropic ADPs and (b) structural disorder for Cu atoms.

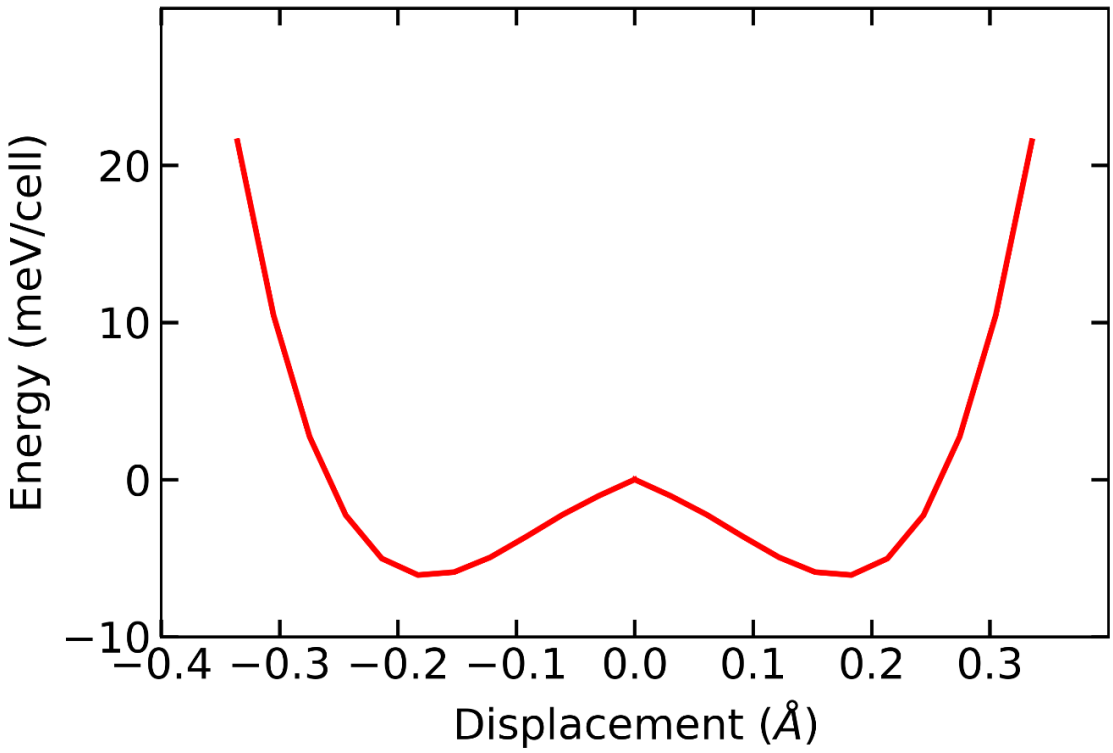

Fig. S4 The calculated potential energy surface with a double-well structure for the unstable phonon modes.

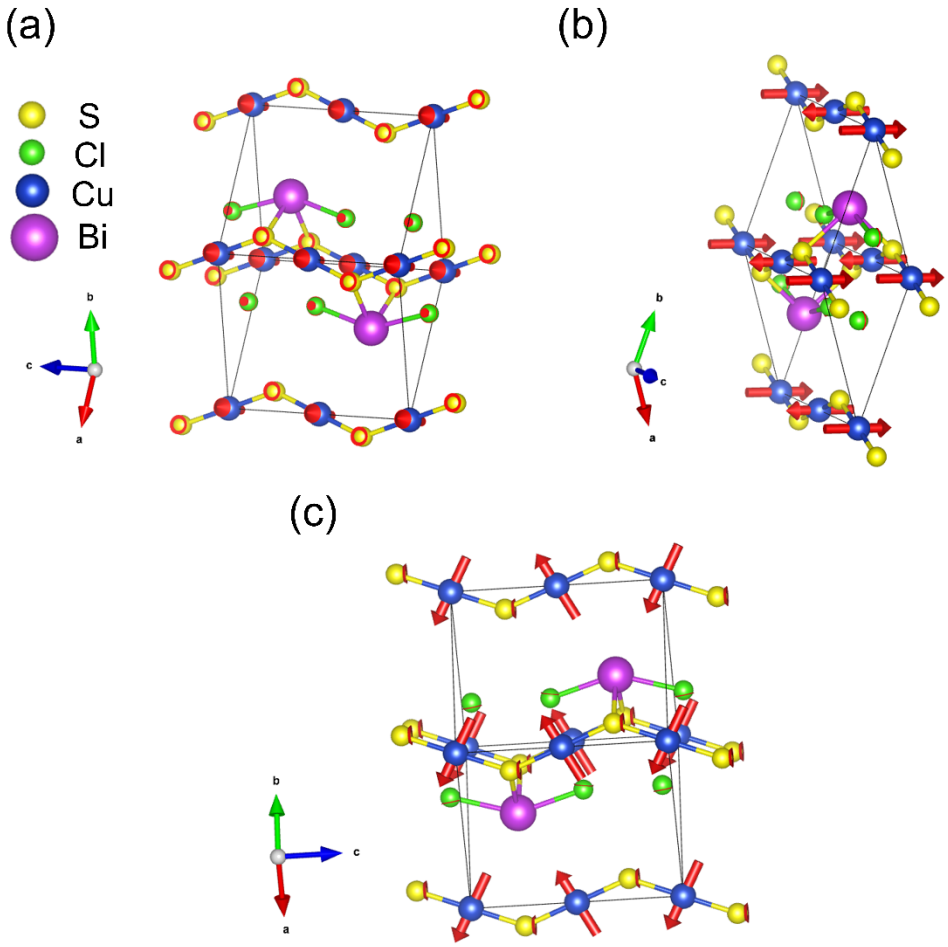

Fig. S5 Visualizations of the unstable modes of (a) -38 cm^{-1}, (b) -29 cm^{-1}, and -15 cm^{-1} at Γ point. The black box represents the primitive unit cell. Blue, magenta, yellow, and green spheres represent Cu, Bi, S, and Cl atoms, respectively.

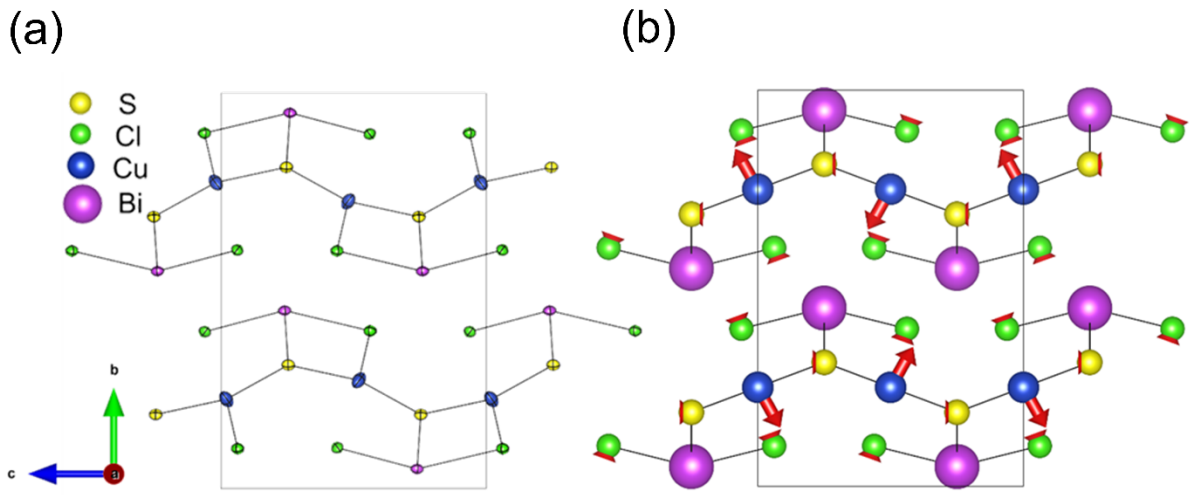

Fig. S6 (a) $CuBiSCl_2$ structure at 80 K with thermal ellipsoid, (b) Visualization of symmetry adapted modes Y_2^-. Blue, magenta, yellow, and green spheres represent Cu, Bi, S, and Cl atoms, respectively.

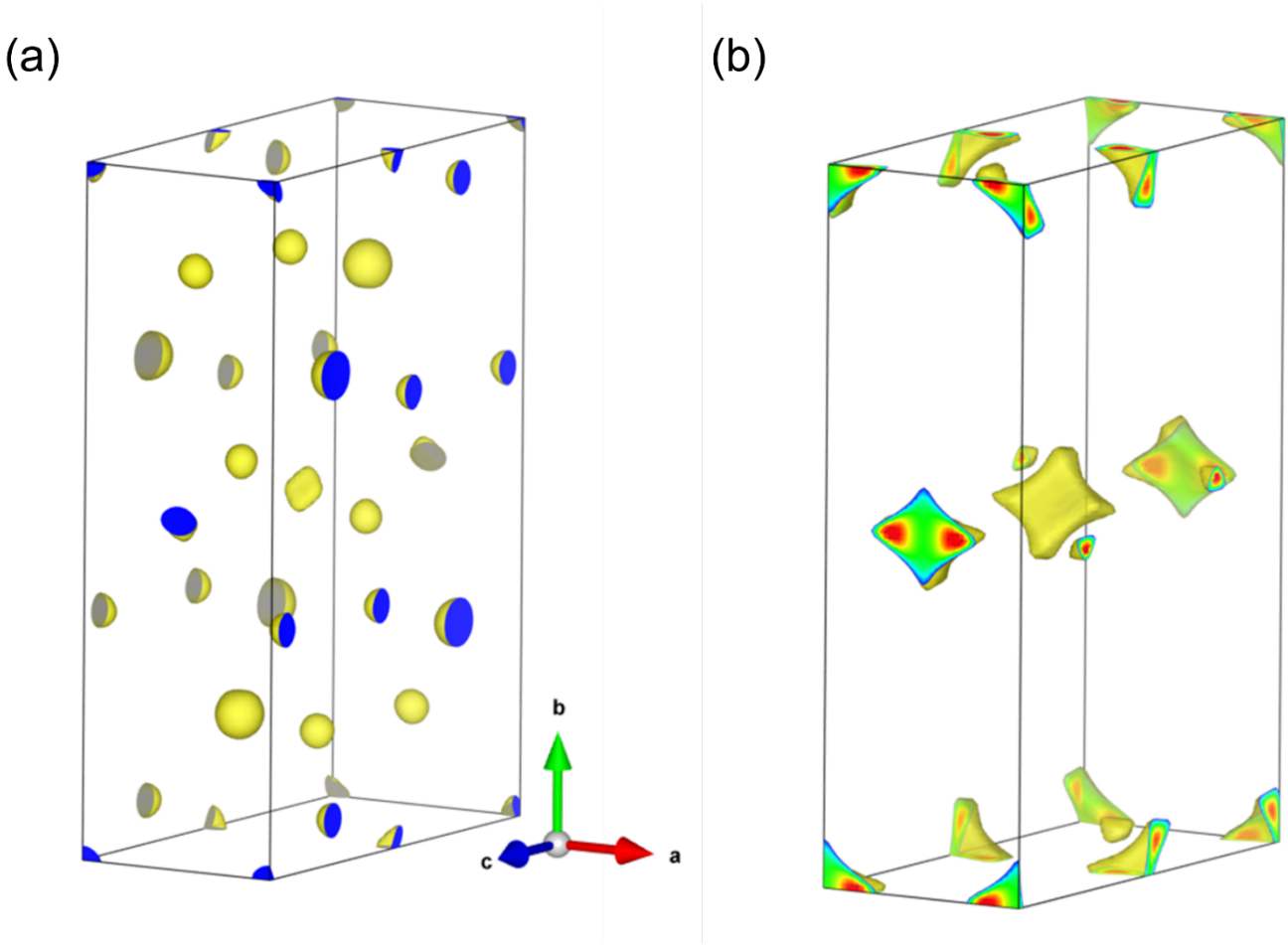

Fig. S7 Part (a) MEM map, Part (b) Bond Valence energy landscape

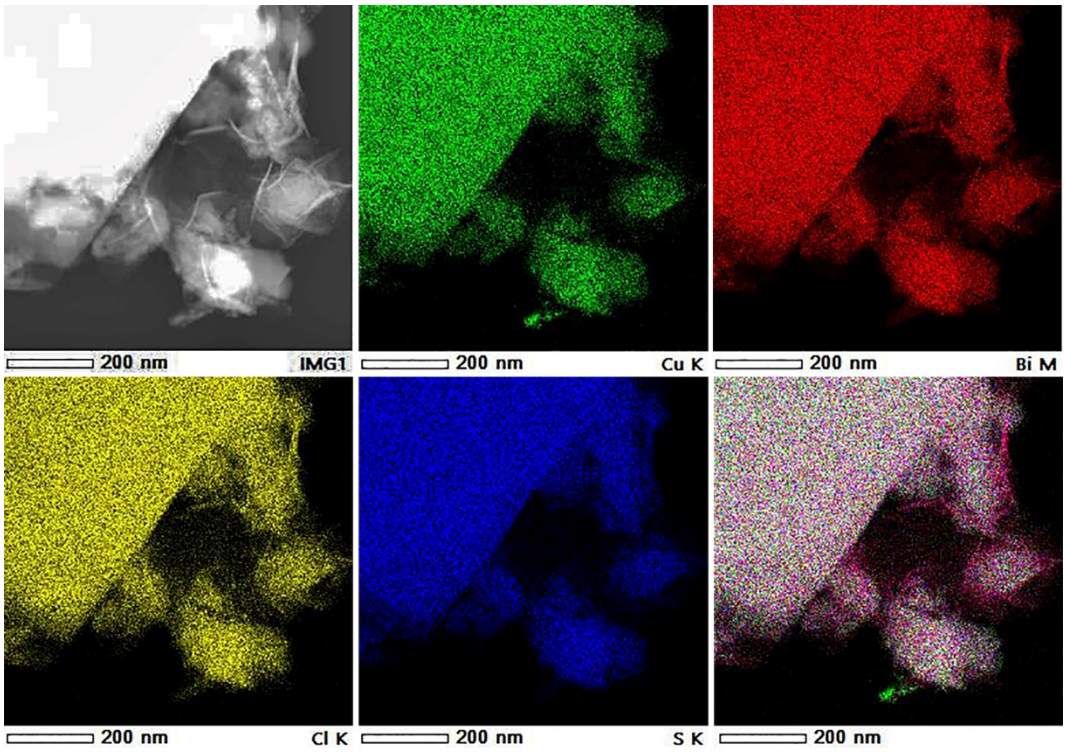

Fig. S8 Low magnification HAADF-STEM image and simultaneously acquired EDX-STEM chemical elements maps of $CuBiSCl_2$ for Cu K, Bi M, Cl K, S K, and overlay color image. Notice homogeneous distribution of all elements within material.

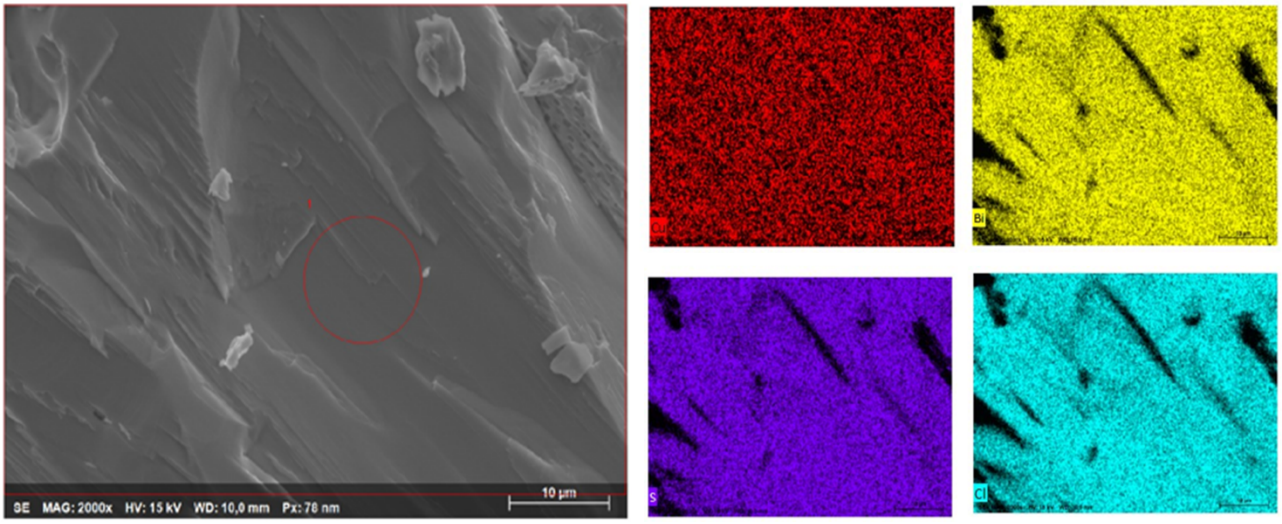

Fig. S9 The SEM and EDS images of a fractured surface of the SPS-ed $CuBiSCl_2$ sample.

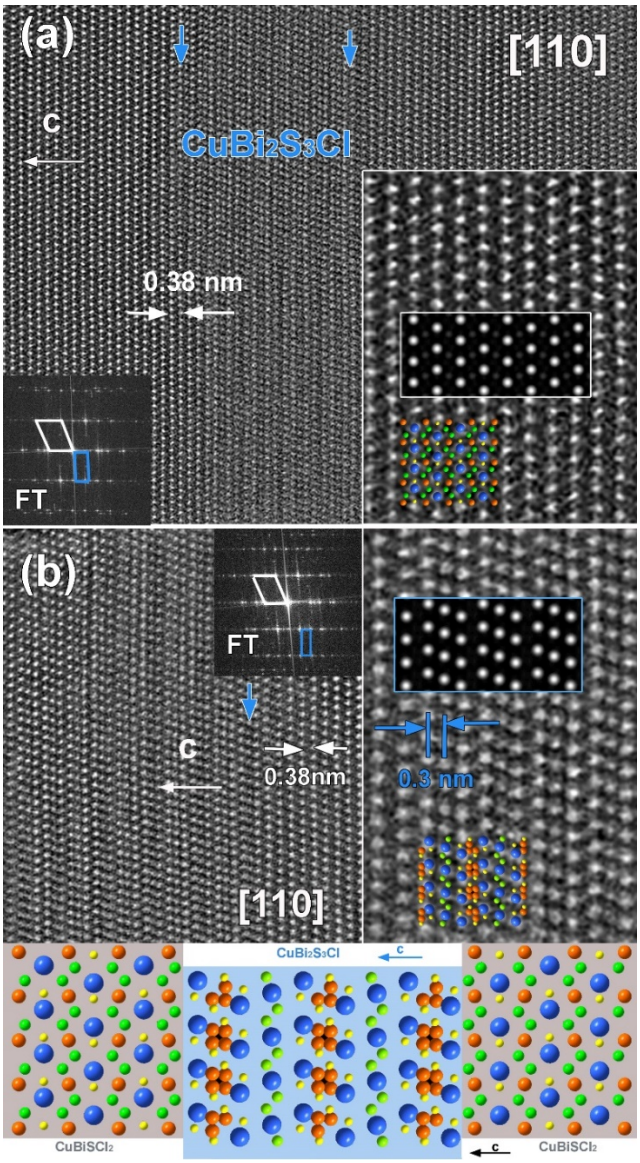

Fig. S10(a) [110] HAADF-STEM image of $CuBiSCl_2$ structure and corresponding FT pattern. Inset shows an enlarged image with overlay image simulation and structural model (Bi-blue, Cu-orange, S-yellow, Cl-green). The blue arrows indicate $CuBi_2S_3Cl$ intergrowth region. (b) HAADF-STEM image of $CuBi_2S_3Cl/CuBiSCl_2$ intergrown layer and corresponding FT pattern. White and blue frames correspond to the unit cell of $CuBiSCl_2$ and $CuBi_2S_3Cl$ phases, respectively. Right panel show an enlargement image of $CuBi_2S_3Cl$ region with overlay structure model (Bi-blue, Cu-orange, S-yellow, Cl-green) and simulated image based on $CuBi_2S_3Cl$ monoclinic *C12/m1* structure (ISCD 127157). Intergrowth $CuBiSCl_2/CuBi2S_3Cl/ CuBiSCl_2$ structure model is shown in the bottom part.

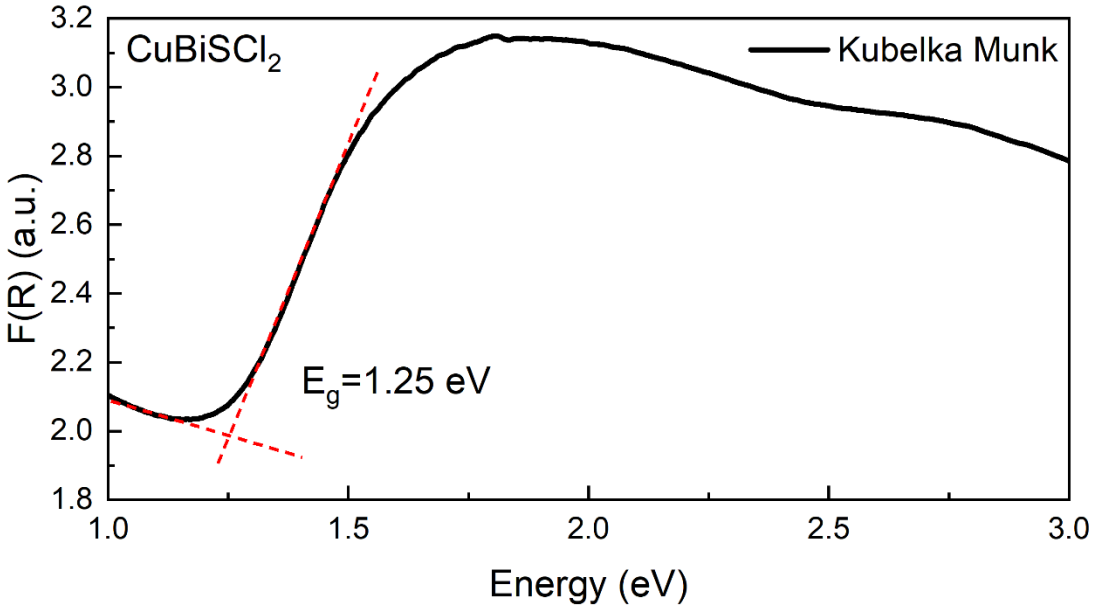

Fig. S11 Kubelba-Munk transforma obtained from the diffuse reflectance spectra. The determination of the optical bandgap was conducted by intersecting tangents at the absorption thresholds.

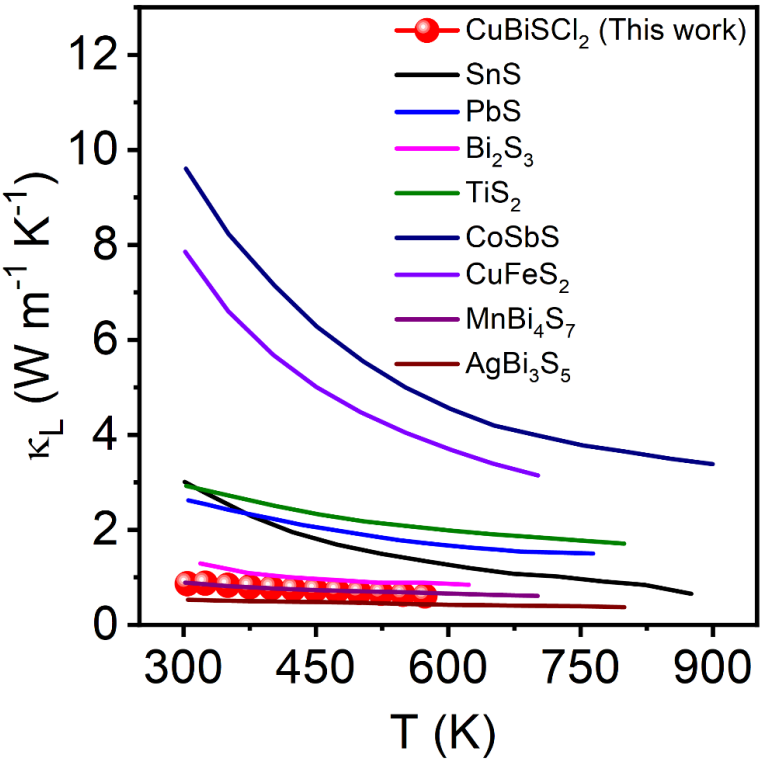

Fig. S12 Comparison κ_L of $CuBiSCl_2$ with single-anion sulfides.

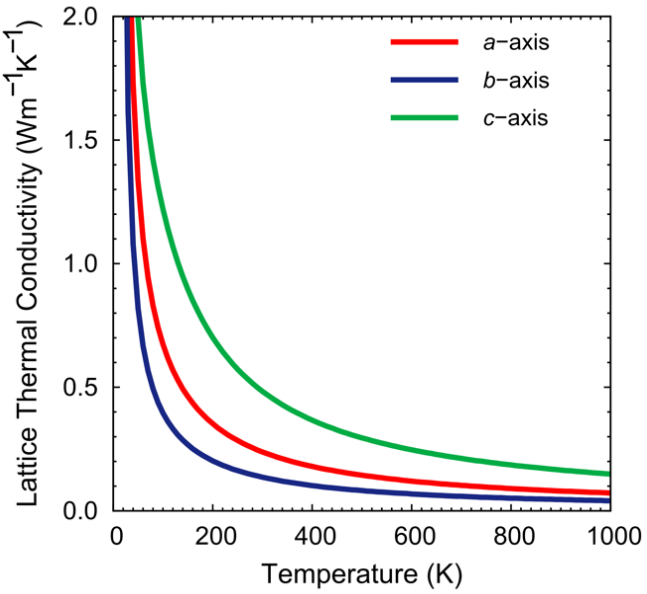

Fig. S13 Temperature dependence of calculated lattice thermal conductivity of Cu_2BiSCl_2 in each axis.

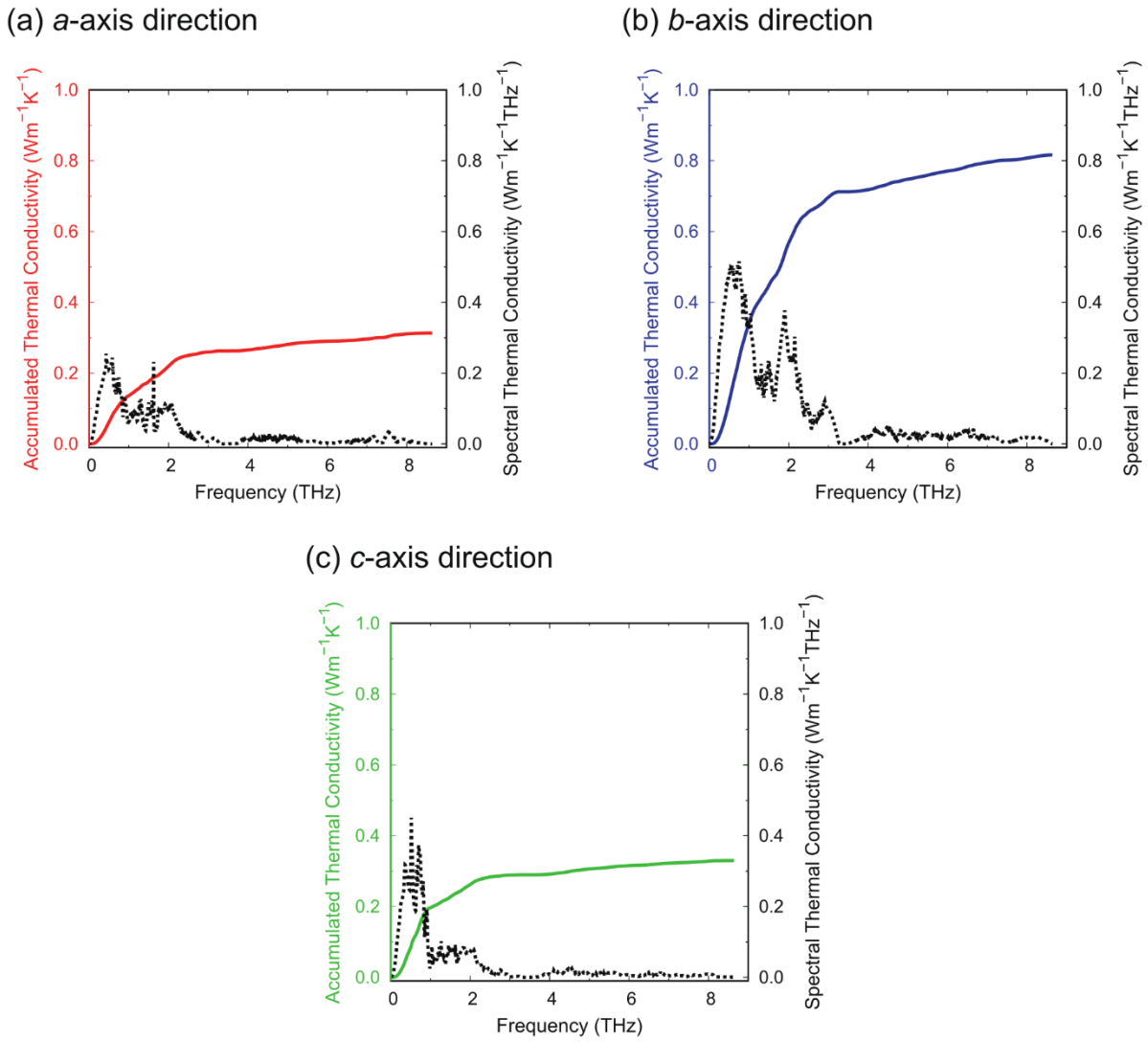

Fig. S14 Accumulated and spectral lattice thermal conductivity of $CuBiSCl_2$ at 300 K in each axis. Colored solid and black dotted lines indicate accumulated and spectral thermal conductivity, respectively.

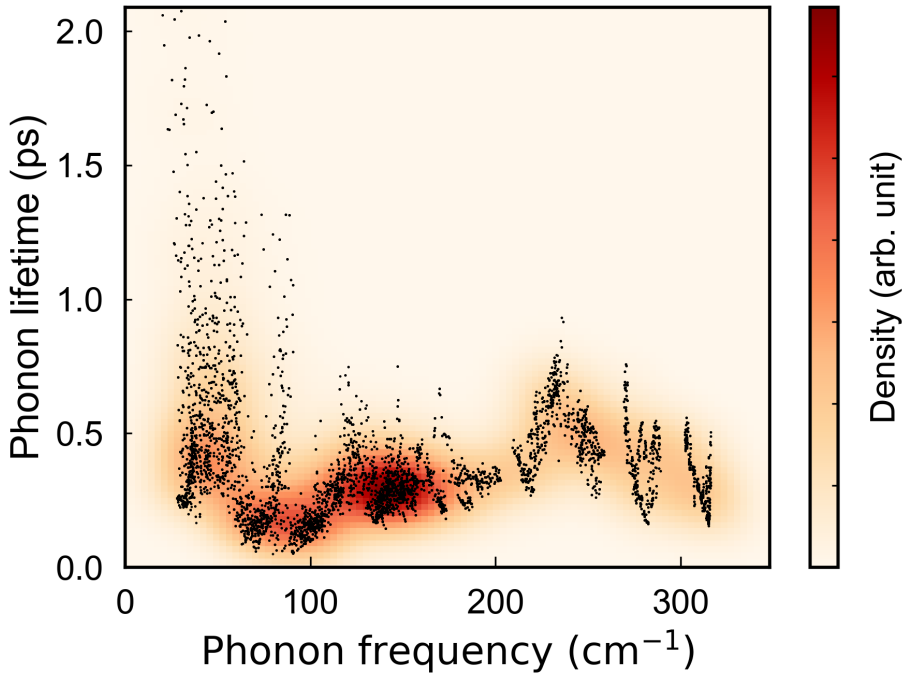

Fig. S15 Phonon lifetime as a function of phonon frequency in $CuBiSCl_2$ at 300 K. Black point indicate lifetime of phonon modes, sampled with a *q*-point mesh of 9×9×9 for the first Brillouin zone. Density of phonon modes are indicated by the color bar.

Table S1. Refined crystallographic data of $CuBiSCl_2$ *Cmcm* phase for the SPS-ed powder at 300 K.

Space Group *Cmcm*, a = 3.9663(1) Å, b=12.8108(2) Å, c =8.6019(1) Å V = 437.08(1) Å^3, Z = 4					
Atom	x	y	z	U_{iso} (Å^2)	Occ.
Cu	0	0	0	0.0788(19)	1
Bi	0	0.70053(8)	0.25	0.0151(3)	1
S	0	0.0584(4)	0.25	0.010(2)	1
Cl	0	0.3539(3)	0.0565(4)	0.0280(16)	1

Table S2. $CuBiSCl_2$ structural parameters obtained from single crystal XRD at 80 K.

Space Group *P*2$_1$*cn*, *a* = 3.95549(14) Å, *b* = 12.77520 (40) Å, *c* = 8.56500(30) Å					
R(obs)=3.52, R(all)= 4.12, wR(all)=9.62, GoF(obs)=1.92					
measured / observed [I>3**σ**(I)] reflections=1880/ 1607, 46 refined parameters					
Atom	**x**	**y**	**z**	**occ.**	**adp**
Bi1	-0.59497(12)	0.549824(19)	0.76024(3)	1	0.01421(8)
Cl1	-0.607(2)	0.60113(13)	0.4374(2)	1	0.0156(4)
Cl2	-0.6035(19)	0.60332(13)	1.0614(2)	1	0.0155(4)
S3	-0.1160(12)	0.68748(16)	0.7464(2)	1	0.0136(5)
Cu1	-0.1037(9)	0.77408(10)	0.97970(13)	1	0.0276(3)

ADP anisotropic parameters (Å^2)						
Atom	**U11**	**U22**	**U33**	**U12**	**U13**	**U23**
Bi1	0.01303(15)	0.01237(12)	0.01723(14)	-0.00133(18)	-0.0025(3)	0.00010(7)
Cl1	0.0171(9)	0.0137(6)	0.0160(7)	0.002(2)	-0.001(2)	-0.0005(5)
Cl2	0.0172(8)	0.0144(6)	0.0150(7)	0.004(2)	0.006(2)	0.0004(5)
S3	0.0117(12)	0.0125(6)	0.0166(8)	0.0028(12)	0.0016(16)	0.0000(5)
Cu1	0.0321(7)	0.0285(5)	0.0222(5)	0.0112(14)	-0.0021(13)	-0.0093(4)

Table S3. Experimental sound velocity and elastic properties of $CuBiSCl_2$ at 300 K.

Composition	v_l (m/s)	v_t (m/s)	$v_{a,exp}$ (m/s)	v_p	E (GPa)	G (GPa)	Υ
$CuBiSCl_2$	3116	1450	1633	0.36	38.3	8.1	2.23

Table S4. Fitting parameters of the measured κ_L using Debye-Callaway model.

Composition	m	L (μm)	Θ_D (K)	A ($\times 10^{-40}$)	$v_{a,exp}$ (m/s)
$CuBiSCl_2$	3	2	194	1.5	1633

Table S5. Fitting parameters of low-temperature C_p of $CuBiSCl_2$.

Composition	γ (J mol^{-1} K^{-2})	β ($\times 10^{-4}$ J mol^{-1} K^{-4})	Θ_D (K)	A1 (J mol^{-1} K^{-1})	Θ_{E1} (K)	A2 (J mol^{-1} K^{-1})	Θ_{E2} (K)
$CuBiSCl_2$	0.011(4)	1.9(2)	194	11.3(2)	50(2)	27(2)	94(6)

References

1. Rodríguez-Carvajal, J., Recent Advances in magnetic structure determination by neutron powder diffraction. *Physica B: Condensed Matter* **1993,** *192* (1), 55-69.
2. Roisnel, T.; Rodríquez-Carvajal, J., WinPLOTR: A Windows Tool for Powder Diffraction Pattern Analysis. *Materials Science Forum* **2001,** *378-381*, 118-123.
3. Ruck, M.; Poudeu Poudeu, P. F.; Söhnel, T., Synthese, Kristallstruktur und elektronische Bandstruktur der isotypen Sulfidchloride $CuBiSCl_2$ und $AgBiSCl_2$. *Zeitschrift für anorganische und allgemeine Chemie* **2004,** *630* (1), 63-67.
4. Palatinus, L.; Chapuis, G., SUPERFLIP - a computer program for the solution of crystal structures by charge flipping in arbitrary dimensions. *Journal of Applied Crystallography* **2007,** *40* (4), 786-790.
5. Petříček, V.; Palatinus, L.; Plášil, J.; Dušek, M., Jana2020 – a new version of the crystallographic computing system Jana. **2023,** *238* (7-8), 271-282.
6. Smeets, S.; Wang, B.; Maier, J.; Hogenbirk, E., *instamatic-dev/instamatic: 1.7.0* **2021**.
7. Palatinus, L.; Brazda, P.; Jelinek, M.; Hrda, J.; Steciuk, G.; Klementova, M., Specifics of the data processing of precession electron diffraction tomography data and their implementation in the program PETS2.0. *Acta Crystallographica Section B* **2019,** *75* (4), 512-522.
8. Momma, K.; Ikeda, T.; Belik, A. A.; Izumi, F., Dysnomia, a computer program for maximum-entropy method (MEM) analysis and its performance in the MEM-based pattern fitting. *Powder Diffraction* **2013,** *28* (3), 184-193.
9. Katcho, N. A.; Carrete, J.; Reynaud, M.; Rousse, G.; Casas-Cabanas, M.; Mingo, N.; Rodriguez-Carvajal, J.; Carrasco, J., An investigation of the structural properties of Li and Na fast ion conductors using high-throughput bond-valence calculations and machine learning. *Journal of Applied Crystallography* **2019,** *52* (1), 148-157.
10. Alleno, E.; Bérardan, D.; Byl, C.; Candolfi, C.; Daou, R.; Decourt, R.; Guilmeau, E.; Hébert, S.; Hejtmanek, J.; Lenoir, B.; Masschelein, P.; Ohorodnichuk, V.; Pollet, M.; Populoh, S.; Ravot, D.; Rouleau, O.; Soulier, M., Invited Article: A round robin test of the uncertainty on the measurement of the thermoelectric dimensionless figure of merit of $Co_{0.97}Ni_{0.03}Sb_3$. *Review of Scientific Instruments* **2015,** *86* (1), 011301.
11. Kresse, G.; Furthmüller, J., Efficiency of ab-initio total energy calculations for metals and semiconductors using a plane-wave basis set. *Computational Materials Science* **1996,** *6* (1), 15-50.
12. Kresse, G.; Furthmüller, J., Efficient iterative schemes for ab initio total-energy calculations using a plane-wave basis set. *Physical Review B* **1996,** *54* (16), 11169-11186.
13. Blöchl, P. E., Projector augmented-wave method. *Physical Review B* **1994,** *50* (24), 17953-17979.
14. Kresse, G.; Joubert, D., From ultrasoft pseudopotentials to the projector augmented-wave method. *Physical Review B* **1999,** *59* (3), 1758-1775.
15. Perdew, J. P.; Ruzsinszky, A.; Csonka, G. I.; Vydrov, O. A.; Scuseria, G. E.; Constantin, L. A.; Zhou, X.; Burke, K., Restoring the Density-Gradient Expansion for Exchange in Solids and Surfaces. *Physical Review Letters* **2008,** *100* (13), 136406.
16. Grimme, S.; Antony, J.; Ehrlich, S.; Krieg, H., A consistent and accurate ab initio parametrization of density functional dispersion correction (DFT-D) for the 94 elements H-Pu. *The Journal of Chemical Physics* **2010,** *132* (15), 154104.
17. Togo, A.; Tanaka, I., First principles phonon calculations in materials science. *Scripta Materialia* **2015,** *108*, 1-5.
18. Setyawan, W.; Curtarolo, S., High-throughput electronic band structure calculations: Challenges and tools. *Computational Materials Science* **2010,** *49* (2), 299-312.
19. Nye, J. F., *Physical properties of crystals: their representation by tensors and matrices*. Oxford university press: 1985.
20. Dronskowski, R.; Bloechl, P. E., Crystal orbital Hamilton populations (COHP): energy-resolved visualization of chemical bonding in solids based on density-functional calculations. *The Journal of Physical Chemistry* **1993,** *97* (33), 8617-8624.
21. Deringer, V. L.; Tchougréeff, A. L.; Dronskowski, R., Crystal Orbital Hamilton Population (COHP) Analysis As Projected from Plane-Wave Basis Sets. *The Journal of Physical Chemistry A* **2011,** *115* (21), 5461-5466.

22. Togo, A.; Chaput, L.; Tanaka, I., Distributions of phonon lifetimes in Brillouin zones. *Physical Review B* **2015,** *91* (9), 094306.
23. Togo, A.; Chaput, L.; Tadano, T.; Tanaka, I., Implementation strategies in phonopy and phono3py. *Journal of Physics: Condensed Matter* **2023,** *35* (35), 353001.
24. Monkhorst, H. J.; Pack, J. D., Special points for Brillouin-zone integrations. *Physical Review B* **1976,** *13* (12), 5188-5192.